



Effective use of photogenerated electrons and holes in a system: Photocatalytic selective oxidation of aromatic alcohols to aldehydes and hydrogen production



Sugang Meng^a, Xiangju Ye^b, Jinghu Zhang^a, Xianliang Fu^a, Shifu Chen^{a,b,*}

^a College of Chemistry and Materials Science, Huaibei Normal University, Huaibei 235000, Anhui, People's Republic of China

^b College of Chemistry and Material Engineering, Anhui Science and Technology University, Fengyang 233100, Anhui, People's Republic of China

ARTICLE INFO

Article history:

Received 25 June 2018

Revised 18 August 2018

Accepted 3 September 2018

Keywords:

Visible light

Photocatalysis

Selective oxidation

Aromatic alcohols

Hydrogen evolution

ABSTRACT

Effective utilization of photogenerated electrons and holes in a system is always a research hotspot. Photocatalysis has been identified as a promising solution to tackle the current environmental and energy issues. However, photogenerated holes or electrons were wasted in the traditional photocatalytic process. In the paper, a dual-function photocatalytic reaction system was constructed using dispersed Pt_x-modified 2D-3D Zn₃In₂S₆ hierarchical structures (x = 1–4). In the system, aromatic alcohols were photocatalytically selectively oxidated into aldehydes and protons were reduced to hydrogen by photogenerated holes and electrons, respectively. In the reaction process, one aromatic alcohol is first dehydrogenated into aromatic aldehyde and two H⁺ via the corresponding carbon-centered radical by consuming of two holes, and then two H⁺ ions dehydrogenated from OH group and α C–H of alcohol are evolved into H₂ by depleting of two electrons. Atomically dispersed Pt_x could offer the maximum atom efficiency and significantly promote visible light absorption and separation of photogenerated electron-hole pairs. The cooperative photoredox system exhibits remarkable photocatalytic activity for visible light-driven splitting of aromatic alcohols. Under visible light irradiation for 6 h, The H₂ output over 2.14% Pt/Zn₃In₂S₆ reaches up to 950 μmol, which is around 7.5, 5.3 and 3.8 times higher than that over Zn₃In₂S₆, Pt-nanoparticle/Zn₃In₂S₆ and MoS₂/Zn₃In₂S₆, respectively. The apparent quantum efficiency (AQE) of 2.14% Pt/Zn₃In₂S₆ at 400 nm is about 4.6%. The utilization rate of photogenerated electrons to holes could be achieved 98.2%. Moreover, Pt/Zn₃In₂S₆ hybrid shows high stability even when Zn₃In₂S₆ was stored for 12 months. Compared with two half-reactions: the photocatalytic selective organics transformation under O₂ atmosphere and the water splitting with sacrificial reagents, such designed dual-purpose photocatalytic reaction not only could effective use of photogenerated electrons and holes for organics transformation and hydrogen production simultaneously but also shows much higher photocatalytic activity than two half-reactions. At the same time, the work also expands the research field of photocatalysis, such as N₂ fixation and CO₂ reduction by using of the as-produced H⁺.

© 2018 Published by Elsevier Inc.

1. Introduction

To address the challenges of impending global energy needs and worsening environmental problems, conversion of solar energy into sustainable H₂ by photocatalytic splitting of water has been identified as a promising solution and has attracted more and more global attention [1–7]. Although great progress has been achieved in designing photocatalyst and understanding the microscopic mechanism, photocatalytic H₂ evolution still faces many chal-

lenges for practical application [8–17]. For example, the use of sacrificial reagents undesirably wastes the energy of holes, increases the system cost and brings along some oxidation products such as CO₂ [18–20]. How to realize highly efficient production of H₂ along with its intrinsic clean, non-carbon feature and effective use of holes is still a huge challenge.

Recent progresses on photocatalytic selective organic transformations have demonstrated that this green and promising technology can obtain diversiform fine chemicals by selecting appropriate photocatalysts and fine control of reaction conditions [21–24]. For instance, aromatic alcohols could be efficaciously converted into aldehydes by holes photogenerated on visible-light-driven photocatalyst with appropriate conduction band position under mild

* Corresponding author at: College of Chemistry and Materials Science, Huaibei Normal University, Huaibei 235000, Anhui, People's Republic of China.

E-mail address: chshifu@chnu.edu.cn (S. Chen).

conditions [24–29]. It is preferable to the conventional synthetic pathways (strong chemical oxidants (e.g., Cr^{VI} , ClO^- and Cl_2), environment unfriendly heavy metal catalysts, and harsh reaction conditions such as high temperature and high pressure) [27–35].

Consequently, construction of a dual-function photocatalytic reaction system composed of a dehydrogenation of alcohols and a H_2 evolution may be an ideal approach to solve the above problems. In the system, the photogenerated holes are utilized for selective dehydrogenation of alcohols into corresponding aldehydes and H^+ , and the produced H^+ are reduced by the photogenerated electrons to form H_2 . This cooperative photoredox reaction not only offers us a promising avenue to reducing the overall cost of water splitting by simultaneously recovering sustainable energy H_2 and high-value fine chemicals, but also provides a new horizon for direct use of photogenerated electrons and holes. Moreover, this reaction ($\Delta G = 28 \text{ kJ mol}^{-1}$) requires much less energy than water splitting reaction ($\Delta G = 238 \text{ kJ mol}^{-1}$) [36]. Therefore, compared to the photocatalytic selective organic transformation under O_2 atmosphere and the water splitting with sacrificial reagents, such designed dual-purpose photocatalytic reaction system could be more feasible and practical in the perspective of the sustainable development of the whole human society. However, little success has been realized because of the difficulty in controlling the selectivity of hole-induced oxidation [18,19,36–40]. For example, under sunlight irradiation, Pt/CdS favored dehydrogenation (88.9%) over hydrogenolysis to produce H_2 , whereas Pd/CdS_{0.4}Se_{0.6} favored hydrogenolysis (75%) over dehydrogenation to form toluene [36]. Although Pt/TiO₂ [18,37,38] and Pd-nanocubes/TiO₂-nanosheets [19] showed high selectivity for simultaneous 2,3-butanediol (1,1-dibutoxybutane or 1,1-diethoxyethane) production and H_2 evolution under 300 W high-pressure Hg-lamp ($\lambda = 365 \text{ nm}$) and UV-vis light ($300 \text{ nm} \leq \lambda \leq 800 \text{ nm}$), respectively, up to now, few of literatures have been reported visible-light-driven heterogeneous photocatalytic splitting alcohols into corresponding aldehydes and H_2 in a stoichiometric manner [40]. Therefore, to realize simultaneously photocatalytic dehydrogenation of alcohols into H_2 and corresponding aldehydes with high selectivity under visible light irradiation in one photocatalytic reaction system is still a worthy research area. Moreover, exploring the reaction mechanism is also necessary to design photocatalysts with high performance (selectivity, quantum efficiency and stability) for practical applications as early as possible and expand the research field of photocatalysis such as reduction of carbon dioxide and nitrogen fixation.

Herein, we report a multi-function photocatalytic reaction system for simultaneous decorating atomic Pt_x ($x = 1-4$) onto 2D-3D Zn₃In₂S₆ hierarchical structure and visible-light-driven splitting of aromatic alcohols into hydrogen and corresponding aldehydes at room temperature. Zn₃In₂S₆ is a visible-light-absorbing semiconductor with a bulk electronic band gap of about 2.8 eV [41,42]. The Zn₃In₂S₆ valence band (VB) has a potential of 1.9 V (vs. NHE), providing adequate oxidizing capacity for selective oxidation of aromatic alcohols (taking p-methoxybenzyl alcohol as an example, the oxidative potentials of p-methoxybenzyl alcohol/p-methoxybenzaldehyde and p-methoxybenzaldehyde/oxidized p-methoxybenzaldehyde are about 1.56 V and 2.01 V (vs. NHE), respectively) [25,42]. The Zn₃In₂S₆ conduction band (CB) located at about -0.9 V (vs. NHE) has sufficient driving force for H^+ reduction [42,43]. In addition, 3D Zn₃In₂S₆ microspheres assembled by 2D nanosheets are conducive to the deposition of metallic nanoparticles and harvest the induced visible light via multi-layers reflection [44]. Atomically dispersed Pt could offer the maximum atom efficiency and significantly promote separation of photogenerated electron-hole pairs. Therefore, Pt/Zn₃In₂S₆ hybrids exhibit remarkable photocatalytic activity for visible light-driven splitting of aromatic alcohols into hydrogen and corresponding

aldehydes at room temperature. The rates of H_2 evolution and PhCHO production for Pt/Zn₃In₂S₆ are much higher than that of the individual Zn₃In₂S₆, Pt-nanoparticle/Zn₃In₂S₆ and noble metal-free photocatalysts (MoSe₂/Zn₃In₂S₆, MoS₂/Zn₃In₂S₆ and TiN/Zn₃In₂S₆). Moreover, this approach is also suitable for other metal sulfide (such as ZnIn₂S₄ and CdS). The high photocatalytic performance of Pt/Zn₃In₂S₆ hybrids toward visible-light-driven splitting of aromatic alcohols into hydrogen and corresponding aldehydes was investigated by a series of control experiments. The possible mechanism was proposed and proved by electron paramagnetic resonance (EPR) and isotopic tracing experiments.

2. Experimental

2.1. Preparation of photocatalysts

All chemicals used in the experiments were analytical grade and used without further purification. Zn₃In₂S₆ was prepared by a hydrothermal method. In a typical procedure, 0.86 g ZnSO₄·7H₂O, 0.58 g InCl₃·4H₂O, 0.65 g cetyltrimethylammonium bromide and a double excess of CH₃CSNH₂ were dissolved in 70 mL of deionized water. The solution was then transferred into a 100 mL Teflon-lined autoclave and heated at 160 °C for 12 h. After being cooled down to room temperature, the yellow precipitate was washed with absolute ethanol and deionized water for several times. Finally, the obtained sample was dried at 60 °C in a vacuum oven. Pt/Zn₃In₂S₆ photocatalyst was prepared by an in situ photodeposition method. The preparation procedure was the same as that in the activity test.

2.2. Characterization

The X-ray diffraction (XRD) patterns of the as-prepared photocatalysts were tested by a Bruker D8 advance X-ray powder diffractometer with Cu K α radiation at room temperature. The morphologies and microstructures of the photocatalysts were studied by scanning electron microscopy (SEM, FEI Nova Nano 450), transmission electron microscopy (TEM, FEI Tecnai G2 F20) and high-resolution transmission electron microscopy (HRTEM). The X-ray photoelectron spectroscopy (XPS) spectra were measured on a Thermo Scientific ESCA Lab250 spectrometer with an Al K α X-ray beam. Additionally, the binding energies were corrected with reference to C 1s peak at 284.6 eV. UV-vis diffuse reflectance spectroscopy test (DRS) was performed to measure the optical properties of the photocatalysts by a UV-VIS-NIR spectrophotometer (UV-3600, SHIMA-DZU, Japan) with BaSO₄ as a reflectance standard. Photoluminescence (PL) properties were analyzed using a fluorescence spectrometer (RF530, Shimadzu Scientific Instruments Inc., Japan). The values of Pt amount in Pt/Zn₃In₂S₆ photocatalysts were detected by inductively coupled plasma-mass spectrometry (ICP-MS, X-Series 2, Thermo Fisher Scientific, Germany). Electron paramagnetic resonance (EPR) spectra were measured on an EPR Spectrometer (A300, Bruker, Germany). High-angle annual dark-filed scanning transmission electron microscopy (HAADF-STEM) images were obtained on a FEI Titan Themis 200 equipped with a Bruker super-X EDS. The photoelectrochemical tests were carried out on a three-electrode system (CHI-660E, Chenhua Instruments Co., China). A Pt wire and Ag/AgCl were used as counter electrode and reference electrode, respectively. The catalyst powder was deposited on the fluoride tin oxide (FTO) substrate to serve as working electrode (The 4-mg sample was dispersed in 500 μL of deionized water by sonication to get uniform slurry. Then, the 20 μL slurry was deposited as a film on a 0.5 cm \times 0.5 cm FTO substrate. After dry at room temperature, the working electrode was obtained.). A quartz cell

filled with 0.1 M Na₂SO₄ or 0.1 M KCl electrolyte containing 0.1 M K₃[Fe(CN)₆]/K₄[Fe(CN)₆] was used as the reaction system.

2.3. Evaluation of photocatalytic activity

Photocatalytic splitting of aromatic alcohols were performed in a Pyrex top-irradiation reaction vessel connected to a glass-closed gas circulation system. In a typical experiment, 0.18 g Zn₃In₂S₆ powders and 125 μL H₂PtCl₆ solutions (the weight content of Pt in Pt/Zn₃In₂S₆ is 0.54%) were added into 50 mL benzotrifluoride containing 0.2 M benzyl alcohol. The reaction suspension was then degassed by using a mechanical pump and stirred for 30 min in the dark to attain an adsorption-desorption equilibrium. A 300 W Xenon lamp equipped with a 420 nm cutoff filter ($\lambda \geq 420$ nm) was applied as a visible light source. A bandpass filter of 400 nm was used to obtain a 400 nm monochromatic light, the light intensity is 3.43 mW cm⁻², and the irradiation area is about 25 cm². The suspension temperature was controlled at about 10 °C by using a water cooling system. After the reaction, the amount of H₂ generated from the reaction system was measured by using an online gas chromatograph (GC 2014, Shimadzu).

The apparent quantum efficiency (AQE) for hydrogen generation is calculated according to following equation:

$$\text{AQE} = N_e/N_p \times 100\% = (2 \times N_H/N_p) \times 100\% \quad (1)$$

N_e , N_H and N_p are the numbers of reacted electrons, evolved H₂ molecules and incident photons, respectively.

Turnover number (TON) was calculated based on the quantity of H₂ and the quantity of metallic Pt:

$$\text{TON} = (\text{Numbers of evolved H}_2)/(\text{Numbers of metallic Pt}) \quad (2)$$

After reaction, the suspension was centrifuged to obtain the precipitate and the clear liquor. The precipitate was then washed with benzotrifluoride and dried at 60 °C in a vacuum oven. Thus, the photocatalyst Pt/Zn₃In₂S₆ was obtained. The clear liquor was analyzed by a gas chromatograph (GC, Agilent 7890) and gas chromatography-mass spectrometer (GC-MS, Agilent 7890A). Yield of aromatic aldehydes and selectivity for aromatic aldehydes were calculated with following equations:

$$\text{Yield} = (C_{\text{aldehyde}}/C_0) \times 100\% \quad (3)$$

$$\text{Selectivity} = [C_{\text{aldehyde}}/(C_0 - C_{\text{alcohol}})] \times 100\% \quad (4)$$

Here C_0 is the initial concentration of aromatic alcohols; C_{alcohol} and C_{aldehyde} are the concentrations of the residual aromatic alcohols and the corresponding aromatic aldehydes at a certain time after the catalytic reaction, respectively.

According to the theoretical reaction equation, in the photocatalytic splitting of one aromatic alcohol process, one aromatic aldehyde molecule would be formed by consuming of two holes and dehydrogenating of two protons; one H₂ molecule would be produced by consuming of two electrons and two protons. Thus, the utilization rate (R_U) of photogenerated electrons to holes could be calculated with following equation:

$$R_U = (\text{Numbers of evolved H}_2)/(\text{Numbers of aromatic aldehyde}) \times 100\% \quad (5)$$

3. Result and discussion

3.1. Catalyst characterization

3.1.1. XRD analysis

The crystallographic structure and phase purity of the as-synthesized Zn₃In₂S₆ sample were studied by XRD. As shown in

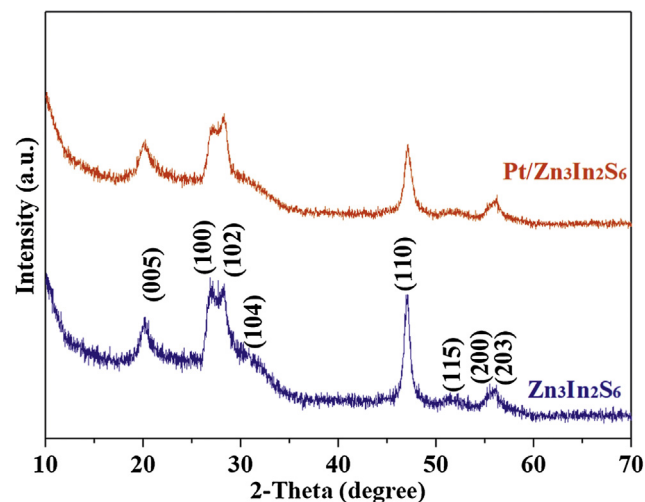


Fig. 1. XRD patterns of pure Zn₃In₂S₆ and 2.14% Pt/Zn₃In₂S₆ hybrid.

Fig. 1, all the XRD peaks of Zn₃In₂S₆ and Pt/Zn₃In₂S₆ can be well indexed to a hexagonal phase of Zn₃In₂S₆ (cell parameters of $a = b = 3.85$ Å, $c = 21.79$ Å, JCPDS No. 24–1453). The peaks located at about 20.3°, 26.7°, 28.1°, 31.5°, 47.1°, 51.8°, 55.1° and 56.5° are attributed to the diffraction of the (0 0 5), (1 0 0), (1 0 2), (1 0 4), (1 1 0), (1 1 5), (2 0 0) and (2 0 3) crystal planes of hexagonal Zn₃In₂S₆, respectively. No other new peaks are observed in the XRD pattern of Zn₃In₂S₆, indicating that the as-prepared Zn₃In₂S₆ is a pure phase. In addition, no peaks belonging to Pt nanocrystal are found in Pt/Zn₃In₂S₆ sample when the weight ratio of Pt is 2.14%, which might be attributed to its low loading amount or small crystalline size. Moreover, it is notable that no peaks belonging to impurities can be found in the XRD pattern of Pt/Zn₃In₂S₆ sample, indicating that Zn₃In₂S₆ keeps pure hexagonal phase, and no impurities are formed in Pt/Zn₃In₂S₆ hybrid. Additionally, the diffraction peaks of Pt/Zn₃In₂S₆ are as broad as that of Zn₃In₂S₆. This indicates that the crystallographic structure of Zn₃In₂S₆ has not been changed after deposition of Pt.

3.1.2. DRS analysis

The light absorption properties of Zn₃In₂S₆ and Pt/Zn₃In₂S₆ samples were detected by UV–vis DRS. As shown in Figs. 2 and S1, it is clear that Zn₃In₂S₆ exhibits a strong absorption edge at about 420 nm. Compared with absorption spectrum of Zn₃In₂S₆, the Pt/Zn₃In₂S₆ hybrid exhibits stronger visible-light absorption. Moreover, the intensity of visible-light absorption increases with increasing Pt amount. It is often attributed to the localized surface plasmon resonance (LSPR) of Pt nanoparticles which depends on its shape, size, and dielectric environment [14]. Herein, the particle size of Pt (about 1.5 nm, see the below analysis) is much smaller than the incident light wavelength, the electric field of light can be almost assumed to be uniform across the Pt nanoparticles. In this situation, the electron oscillation is described in a dipolar electric mode, and the red shift of the absorption for metal-semiconductor composite can be attributed to the near-field scattered light of the semiconductor [11,45]. Therefore, the enhanced visible-light absorption of the Pt/Zn₃In₂S₆ composite can be mainly attributed to the near-field scattered light of the 2D-3D Zn₃In₂S₆ spherically hierarchical structure. Thus, the visible-light driven photoactivity of Zn₃In₂S₆ is expected to be improved by deposition of Pt. It is known that the optical band gap energy (E_g) of a direct band semiconductor Zn₃In₂S₆ and Pt/Zn₃In₂S₆ can be calculated from Kubelka-Munk function: $(F(R)E)^2 = A(E - E_g)$. $F(R)$, E and A are the absorption coefficient, photon energy and proportionality

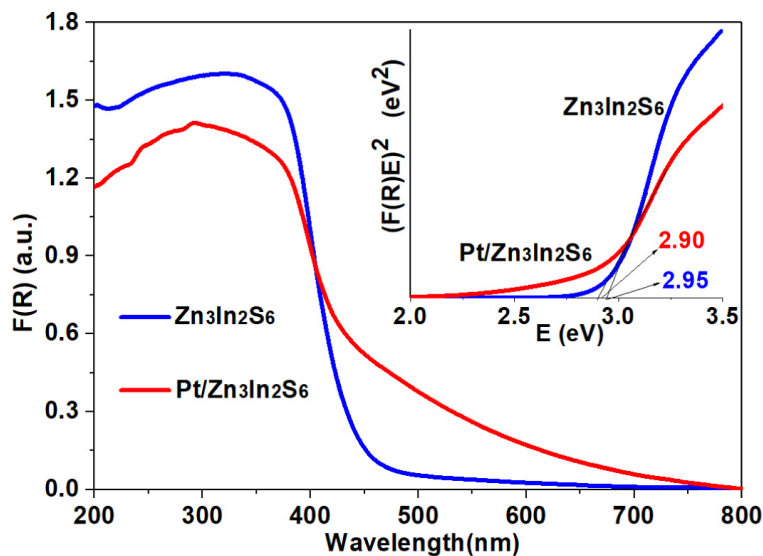


Fig. 2. UV-vis DRS spectra and band gap energies (inset) of pure $\text{Zn}_3\text{In}_2\text{S}_6$ and 2.14% $\text{Pt}/\text{Zn}_3\text{In}_2\text{S}_6$ hybrid.

constant, respectively) [24]. By calculation, the band gap (E_g) of pure $\text{Zn}_3\text{In}_2\text{S}_6$ is 2.95 eV. The band gap of $\text{Zn}_3\text{In}_2\text{S}_6$ is slightly larger than the theoretical value (2.8 eV) [41], which can be attributed to the relatively low-dimensional structure of $\text{Zn}_3\text{In}_2\text{S}_6$ nanoflakes (Fig. 3). Meanwhile, the band gap (E_g) of $\text{Pt}/\text{Zn}_3\text{In}_2\text{S}_6$ is about 2.90 eV. It is clear that, compared with pure $\text{Zn}_3\text{In}_2\text{S}_6$, the $\text{Pt}/\text{Zn}_3\text{In}_2\text{S}_6$ sample may absorb more visible light.

3.1.3. SEM and TEM of pure $\text{Zn}_3\text{In}_2\text{S}_6$

The morphology information and microscopic structure of the as-prepared $\text{Zn}_3\text{In}_2\text{S}_6$ were investigated by SEM and TEM (Fig. 3). It is clear that $\text{Zn}_3\text{In}_2\text{S}_6$ exhibits regular microsphere-like shape with a diameter of about 1–2 μm . The magnified SEM image (inset in Fig. 3A) shows these microspheres with smooth surface are comprised of crisscrossed nanoflakes with thickness of about 10 nm. It indicates that the as-prepared $\text{Zn}_3\text{In}_2\text{S}_6$ sample possesses 3D hierarchical structure by self-assembling of 2D nanoflakes (like marigold). This 2D-3D hierarchical structure can be further confirmed by the TEM images (Fig. 3B and C). The clear lattice fringes of the 2D nanoflakes (Fig. 3D) demonstrate the highly crystalline characteristic of $\text{Zn}_3\text{In}_2\text{S}_6$. The d spacing value of 0.19 nm corresponds to the (1 1 0) crystal plane of the hexagonal $\text{Zn}_3\text{In}_2\text{S}_6$ (JCPDS No. 24-1453). It is coincident with the XRD result (Fig. 1). The energy dispersive X-ray spectroscopy (EDX) equipped on the SEM (Fig. 3E) reveals that the as-prepared $\text{Zn}_3\text{In}_2\text{S}_6$ sample is composed of zinc (Zn), indium (In) and sulfur (S), whereas carbon (C) and oxygen (O) are probably ascribed to the graphite conductive adhesive or the absorbed gaseous molecules. The EDX quantitative analysis gives an average Zn:In:S ratio of 1.76:1:3.15, which is in accordance with the stoichiometry of $\text{Zn}_3\text{In}_2\text{S}_6$. In addition, EDX-mapping analysis (Fig. 3F) performed on SEM indicates that Zn, In and S uniformly enrich the entire microsphere. Based on the above characterization, it is concluded that the $\text{Zn}_3\text{In}_2\text{S}_6$ with hierarchical structure has been successfully synthesized by this facile approach.

3.1.4. SEM, TEM and HAADF-STEM of the $\text{Pt}/\text{Zn}_3\text{In}_2\text{S}_6$ hybrid

The microscopic structure and elementary composition of the typical $\text{Pt}/\text{Zn}_3\text{In}_2\text{S}_6$ hybrid are presented in Fig. 4. It can be seen from Fig. 4A and B that the morphology of $\text{Pt}/\text{Zn}_3\text{In}_2\text{S}_6$ hybrid is also identical to that of $\text{Zn}_3\text{In}_2\text{S}_6$ in general, including 3D spherical shape and 2D layered nanoflakes (marked in Fig. 4C). However,

when the TEM image was magnified 400,000 times (Fig. 4D), many ultrafine Pt particles with diameter of 0.4–1.6 nm dispersed on the (1 1 0) crystal plane of hexagonal $\text{Zn}_3\text{In}_2\text{S}_6$ can be clearly found. Because the diameter of one Pt atom is about 0.366 nm, the ultrafine Pt particles are made up of 1–4 atoms. Thus the ultrafine Pt particles could be called atomically dispersed Pt_x ($x = 1-4$), and that is why no peaks belonging to Pt nanocrystal are found in the XRD pattern of $\text{Pt}/\text{Zn}_3\text{In}_2\text{S}_6$ hybrid. TEM-EDX-mapping analysis was applied to clarify the composition profile of $\text{Pt}/\text{Zn}_3\text{In}_2\text{S}_6$ hybrid. As shown in Fig. 4E and F, besides Zn, In and S, Pt uniformly enriches the entire microsphere of $\text{Pt}/\text{Zn}_3\text{In}_2\text{S}_6$ hybrid, implying that the diameter of Pt is very ultrafine (because of the small amount of Pt, the big particles or aggregation for the distribution of Pt would be not uniform or full of the entire microsphere). Moreover, the EDX spectrum (Fig. 4G) also reveals that the $\text{Pt}/\text{Zn}_3\text{In}_2\text{S}_6$ hybrid is composed of Zn, In, S and Pt, whereas C, O and Cu come from the carbon membrane and copper wire mesh. Furthermore, the dominance of isolated Pt atoms on 2D $\text{Zn}_3\text{In}_2\text{S}_6$ can be confirmed by atomic resolution high-angle annular dark-field scanning transmission electron microscopy (HAADF-STEM) images (Fig. S2). The HAADF-STEM image clearly shows many bright dots of atomic size as highlighted by the red circles, corresponding to heavy Pt atoms with a mean size of ~ 1.5 nm, are well dispersed on the surface of 2D $\text{Zn}_3\text{In}_2\text{S}_6$. It is in accordance with the recent report that a stable atomically dispersed Pd-TiO_2 (Pd_1/TiO_2) was prepared by a photochemical strategy [46]. These results indicate that photodeposition may be an efficient method to prepare metal single-atom materials.

3.1.5. XPS of the $\text{Pt}/\text{Zn}_3\text{In}_2\text{S}_6$ hybrid

To further determine the surface chemical composition and element valence states of $\text{Pt}/\text{Zn}_3\text{In}_2\text{S}_6$ hybrid, the 2.14% $\text{Pt}/\text{Zn}_3\text{In}_2\text{S}_6$ hybrid was characterized by XPS (Fig. 5). The peaks at around 71.2 and 74.5 eV are attributed to metallic Pt^0 (Fig. 5A) [14]. Furthermore, the amount of metallic Pt^0 in 2.14% $\text{Pt}/\text{Zn}_3\text{In}_2\text{S}_6$ hybrid is measured to be about 1.3%, which is consistent with the measurement result of ICP-MS (1.5%). Meanwhile, the high resolution XPS spectra of Zn 2p peaks at 1021.8 and 1044.8 eV (Fig. 5B), In 3d peaks at 445.0 and 452.6 eV (Fig. 5C) and S 2p at 161.8 and 162.9 eV (Fig. 5D) can be assigned to Zn^{2+} , In^{3+} and S^{2-} of $\text{Zn}_3\text{In}_2\text{S}_6$, respectively. The XPS analysis corroborates the presence of metallic Pt^0

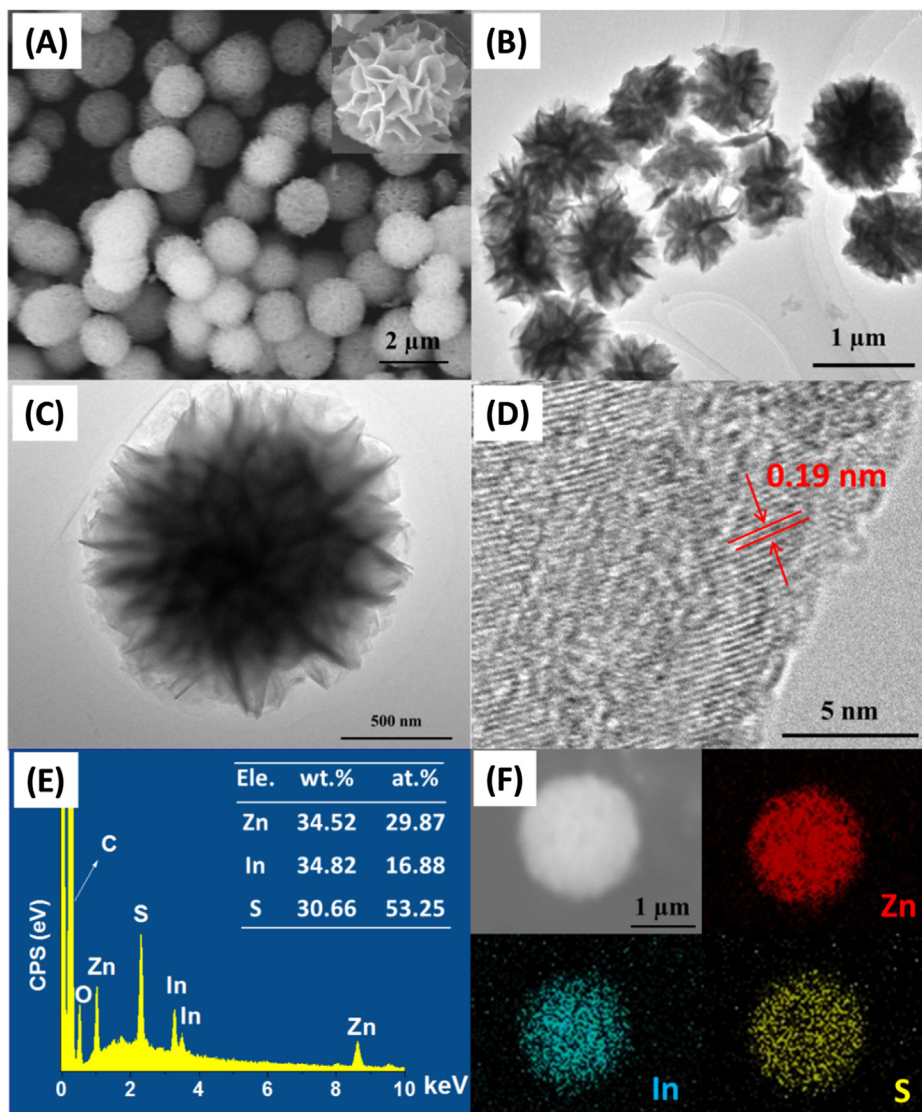


Fig. 3. (A and inset) SEM, (B and C) TEM, (D) HRTEM images, (E) EDX pattern and elemental contents (inset), and (F) EDX-mapping images of $\text{Zn}_3\text{In}_2\text{S}_6$.

in the $\text{Pt}/\text{Zn}_3\text{In}_2\text{S}_6$ hybrid, and demonstrates that the chemical states of $\text{Zn}_3\text{In}_2\text{S}_6$ had no change after deposition of Pt on it.

3.2. Evaluation of photocatalytic activity

The photocatalytic performance of the as-prepared $\text{Zn}_3\text{In}_2\text{S}_6$ photocatalyst was evaluated by the dual-function photocatalytic system toward H_2 evolution along with the selective oxidation of benzyl alcohol into benzaldehyde under mild conditions (visible light irradiation ($\lambda \geq 420$ nm) and temperatures remained at 10°C by using a water cooling system).

The effect of the amount of photocatalyst on the photoactivity was investigated. As exemplified in Fig. 6A, the rates of H_2 evolution and PhCHO production increased along with the increasing amount of $\text{Zn}_3\text{In}_2\text{S}_6$ photocatalyst and then decreased. The optimized amount of $\text{Zn}_3\text{In}_2\text{S}_6$ in the dual-function photocatalytic system was about 0.18 g. The rates of H_2 evolution and PhCHO production for the pure $\text{Zn}_3\text{In}_2\text{S}_6$ photocatalyst are 21.0 and $26.7 \mu\text{mol h}^{-1}$, respectively. The selectivity is about 80%. A similar phenomenon had been reported by others when studying photocatalytic degradation of dyes [47]. This phenomenon can be

explained in terms of availability of active sites on the catalyst surface and the penetration of light into the suspension [47].

Different amounts of H_2PtCl_6 solution were introduced into the photocatalytic system for studying the optimum content of Pt on improving the photoactivity of $\text{Zn}_3\text{In}_2\text{S}_6$ photocatalyst, as shown in Fig. 6B. The photocatalytic H_2 evolution and PhCHO production both display tendencies to increase with increasing Pt content and achieve maximum values at the weight content of 2.14%, indicating that a cooperative interaction between Pt and $\text{Zn}_3\text{In}_2\text{S}_6$ photocatalyst is required to optimally improve the photoactivity of $\text{Zn}_3\text{In}_2\text{S}_6$ photocatalyst. The rates of H_2 evolution and PhCHO production for 2.14% $\text{Pt}/\text{Zn}_3\text{In}_2\text{S}_6$ hybrid can reach up to 158.1 and $165.9 \mu\text{mol h}^{-1}$, respectively, around 7.5 and 6.2 times higher than that of the pure $\text{Zn}_3\text{In}_2\text{S}_6$ sample, respectively. A higher selectivity (>93%) can also be achieved on $\text{Pt}/\text{Zn}_3\text{In}_2\text{S}_6$ hybrid. These indicate that the photoactivity of $\text{Zn}_3\text{In}_2\text{S}_6$ photocatalyst for H_2 evolution and selective oxidation of PhCH₂OH can be significantly enhanced simultaneously by depositing Pt as co-catalyst. Additionally, after keeping $\text{Zn}_3\text{In}_2\text{S}_6$ in a glass vial for 12 months, the photocatalytic activity of 2.14% $\text{Pt}/\text{Zn}_3\text{In}_2\text{S}_6$ hybrid for H_2 evolution ($166.9 \mu\text{mol h}^{-1}$) displays no deactivation (Fig. S3).

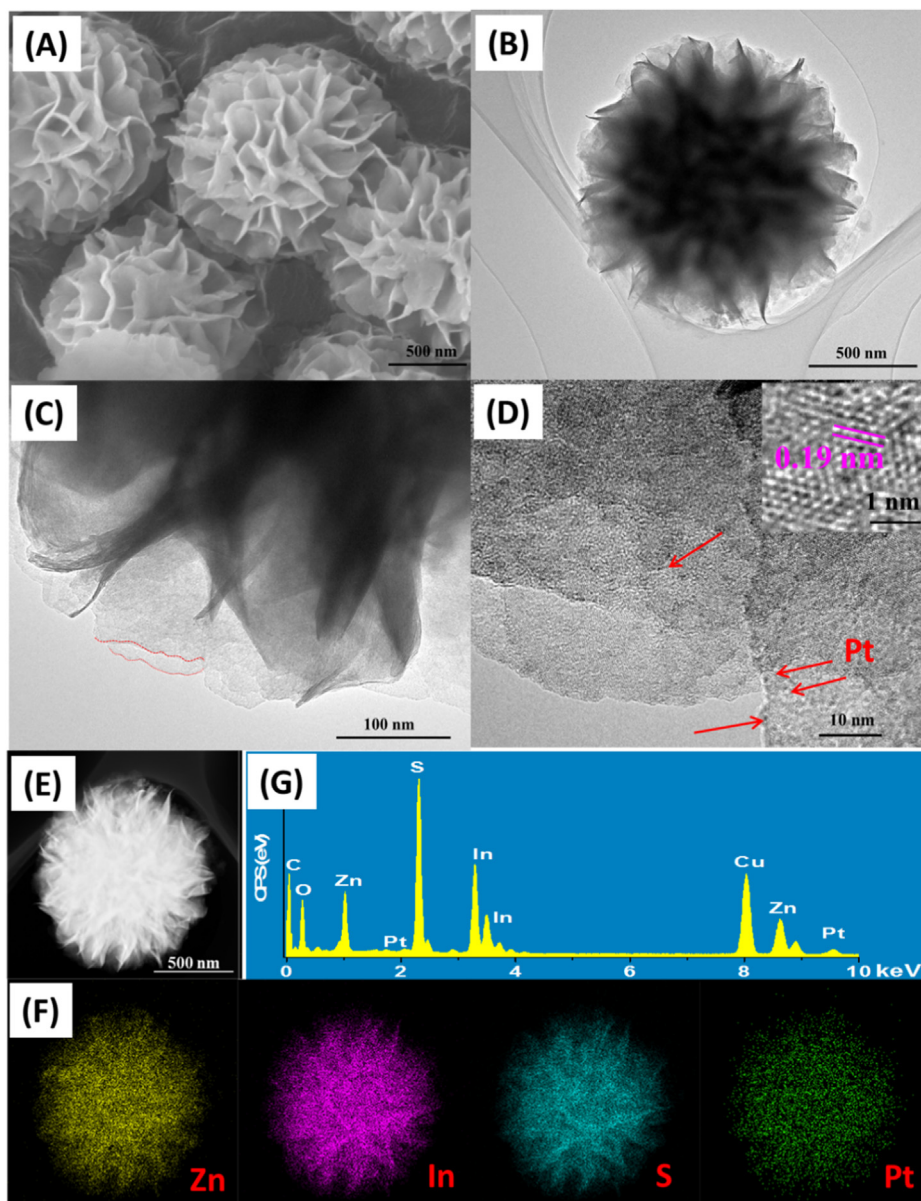


Fig. 4. (A) SEM, (B and C) TEM, (D and inset) HRTEM, (E and F) EDX-mapping images and (G) EDX pattern of the typical Pt/Zn₃In₂S₆ hybrid (2.14% Pt).

To demonstrate the superior of this dual-function reaction system for simultaneous visible light-driven photoredox of aromatic alcohols into hydrogen and corresponding aldehydes by directly using photogenerated electrons and holes, two half-reactions (the photocatalytic selective oxidation of PhCH₂OH under O₂ atmosphere and the water splitting with sacrificial reagents) were performed on 2.14% Pt/Zn₃In₂S₆ hybrid. It is inspiring that 2.14% Pt/Zn₃In₂S₆ hybrid exhibits higher photocatalytic activity in this cooperative photoredox catalysis than in the conventional water splitting using lactic acid as a hole scavenger (the rate of H₂ evolution is about 21.4 μmol h⁻¹) and selective oxidation of PhCH₂OH using O₂ as an electron scavenger (the rate of PhCHO production is about 118.3 μmol h⁻¹) (Figs. S4 and S5).

The primary product for PhCH₂OH oxidation over Pt/Zn₃In₂S₆-photocatalysts is detected by GC-MS (Fig. S6). As shown in Fig. S6a, the peaks at about 7 and 9 min coincide with the peaks of standard PhCHO and PhCH₂OH samples. A peak located at less than 6 min belongs to the impurity of benzotrifluoride solvent. The raw material PhCH₂OH and the product PhCHO can be further

demonstrated by MS spectra. Four strong mass peaks ($m/z = 108, 107, 79$ and 77) labeled at 9 min had been observed and could be attributed to PhCH₂OH (Fig. S6b). While three strong mass peaks ($m/z = 106, 105$ and 77) come from 7 min belong to PhCHO (Fig. S6c). Moreover, No over oxidation products such as PhCOOH in solution were detected by GC-MS; CO₂ in the evolved gas was also not detected by GC.

The utilization rate (R_U) of photogenerated electrons to holes was further investigated by the molar ratio of H₂ and PhCHO. Compared with the pure Zn₃In₂S₆ sample (Fig. 6A), the molar ratio of H₂ and PhCHO over Pt/Zn₃In₂S₆ hybrid is dramatically improved (Fig. 6B). It is similar to the previous reports that metallic Pt⁰ is an effective co-catalyst for photocatalytic splitting of H₂O into H₂ by reducing the over potential of H₂ evolution [13–15]. These indicate that the efficient dual-function photocatalytic system toward H₂ evolution along with the selective oxidation of benzyl alcohol into benzaldehyde under mild conditions can be realized on Pt/Zn₃In₂S₆ hybrid. However, it can be seen that the rate of H₂ evolution is always lower than that of PhCHO production whether

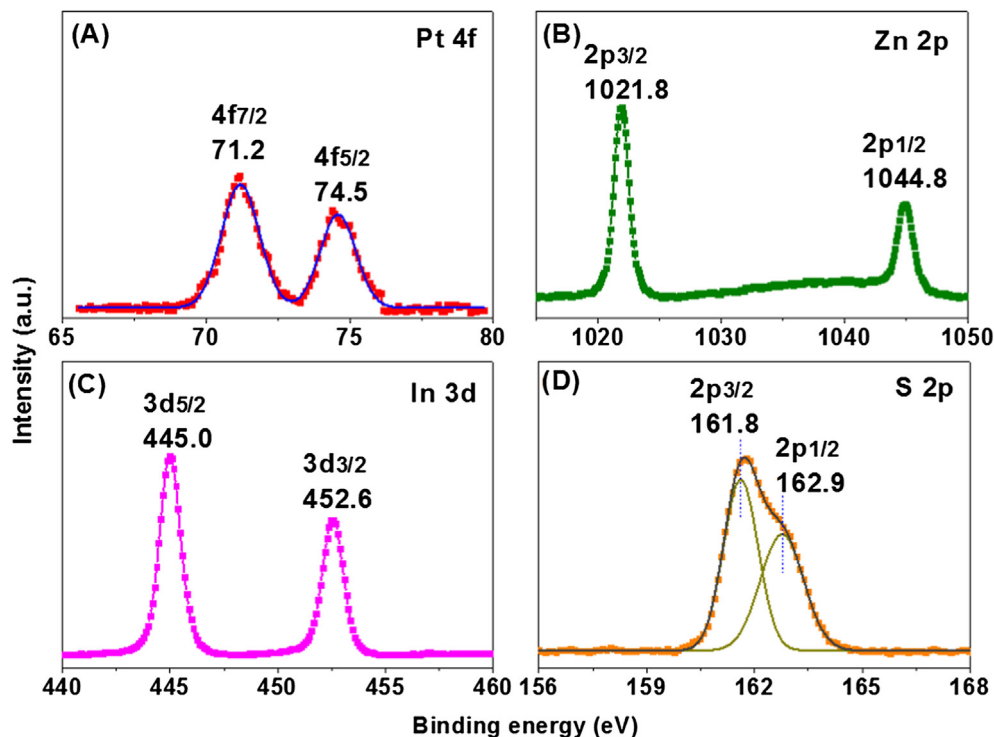


Fig. 5. High-resolution XPS spectra of (A) Pt 4f, (B) Zn 2p, (C) In 3d and (D) S 2p for the 2.14% Pt/Zn₃In₂S₆ sample.

Zn₃In₂S₆ (Fig. 6A) or Pt/Zn₃In₂S₆ hybrid (Fig. 6B). For single Zn₃In₂S₆, because a quantifiable byproduct PhCH₃ had been formed in the photocatalytic process, negligible amount of PhCH₃ were detected in the whole process of photoredox reaction over Pt/Zn₃In₂S₆ hybrid. The result is in line with the recent report that Pt loaded on CdS favors dehydrogenation (evolution of H₂) over hydrogenolysis (selective transformation of PhCH₂OH into PhCH₃) [36]. In this work, preparation of Pt/Zn₃In₂S₆ hybrid and H₂ evolution were performed in one reaction system by an in situ photodeposition method (Zn₃In₂S₆ powder, chloroplatinic acid and PhCH₂OH were simultaneously added into the reaction system. Under visible light irradiation, the photogenerated holes on Zn₃In₂S₆ could oxidize PhCH₂OH into PhCHO and H⁺, while the photoinduced electrons could be trapped by Pt⁴⁺ and H⁺ to form Pt⁰ and H₂, respectively.). Consequently, for Pt/Zn₃In₂S₆ hybrid, it may be mainly caused by the fact that part of the photogenerated electrons are robbed by [PtCl₆]²⁻ ions to form metallic Pt⁰ (competitive process, see TEM and XPS analyses in Figs. 4 and 5). As shown in Fig. 6C, the molar ratio (R_U) of H₂ and PhCHO over Pt/Zn₃In₂S₆ hybrid first increases with the increase of light time and then reaches a plateau. At the beginning of the photocatalytic splitting of benzyl alcohol (1 h), the amount of H₂ (41 μmol) is far lower than that of PhCHO (126 μmol). The R_U is only 32.5%, while R_U increases fast along with the reaction time (1–4 h). At this stage of the reaction, reduction of [PtCl₆]²⁻ ions into metallic Pt⁰ may dominate the reaction, which can be proved by XPS analysis (Fig. 5, about 60.7% [PtCl₆]²⁻ ions were reduced into metallic Pt⁰ after reaction for 6 h) and the obviously enhanced photoactivity. After 6 h, R_U increases slowly, implying the competitive process exists in the photocatalytic reaction. Nevertheless, R_U can reach up to 98.2% at 12 h (that is close to 1), suggesting a stoichiometric cooperative photoredox reaction would be achieved by extending reaction time and photogenerated electrons-holes could be utilized simultaneously and effectively in one reaction system. At this point, 1962.1 μmol H₂ and 1998.3 μmol PhCHO are produced. Therefore, the turnover number (TON) based on the amount of

metallic Pt⁰ is calculated to be about 163.5, and apparent quantum efficiency (AQE) of 4.6% is achieved for H₂ evolution under monochromatic light irradiation at 400 nm.

The relationship between the productions of H₂ evolution and PhCHO generation from PhCH₂OH and the wavelength of incident light was also investigated. As shown in Figs. 6D and S7, the H₂ and PhCHO generation trends match well with 0.54%, 1.14%, 1.74%, 2.14% and 2.74% Pt/Zn₃In₂S₆ optical absorption spectra. It demonstrates that the cooperative photoredox reaction is truly driven by a photocatalysis process on Pt/Zn₃In₂S₆ hybrid. Additionally, the photocatalytic activity of the Pt/Zn₃In₂S₆ hybrid under 600 nm incident light irradiation can be attributed to the hot-electron injection mechanism [45,48].

In addition, to fair evaluate that the atomically dispersed Pt catalyst gives high activity and selectivity, and differs from those of conventional co-catalysts [49–52], Pt-nanoparticles/Zn₃In₂S₆ (Pt-NPs/Zn₃In₂S₆), MoS₂/Zn₃In₂S₆, MoSe₂/Zn₃In₂S₆ and TiN/Zn₃In₂S₆ were prepared by reported procedures (Fig. S8) [53–56]. It is clear that atomic photocatalyst Pt/Zn₃In₂S₆ not only shows higher activity than Pt-NPs/Zn₃In₂S₆, but also presents superior to MoS₂/Zn₃In₂S₆, MoSe₂/Zn₃In₂S₆ and TiN/Zn₃In₂S₆ photocatalysts (Fig. 7). These results strongly suggest that Pt/Zn₃In₂S₆ can be used as an efficient, visible-light-driven photocatalyst toward the photocatalytic selective splitting of aromatic alcohols into clean energy (H₂) and fine chemicals (aromatic aldehydes or ethers) simultaneously under mild reaction conditions.

To extend the general applicability of Pt/Zn₃In₂S₆ hybrid for the photocatalytic selective splitting of aromatic alcohols to H₂ and corresponding aldehydes, a series of aromatic alcohols with different substituent groups (RPhCH₂OH, R = MeO, Me, H, Cl, OH and NO₂) were taken as examples. It can be seen that the Pt/Zn₃In₂S₆ displays higher activity than Zn₃In₂S₆ for photocatalytic splitting of aromatic alcohols (p-methoxybenzyl alcohol, p-methylbenzyl alcohol, p-hydroxybenzyl alcohol, p-chlorobenzyl alcohol and p-nitrobenzyl alcohol) (Fig. S9). In case of several aromatic alcohols with functional groups (Cl, OH and NO₂), the productions

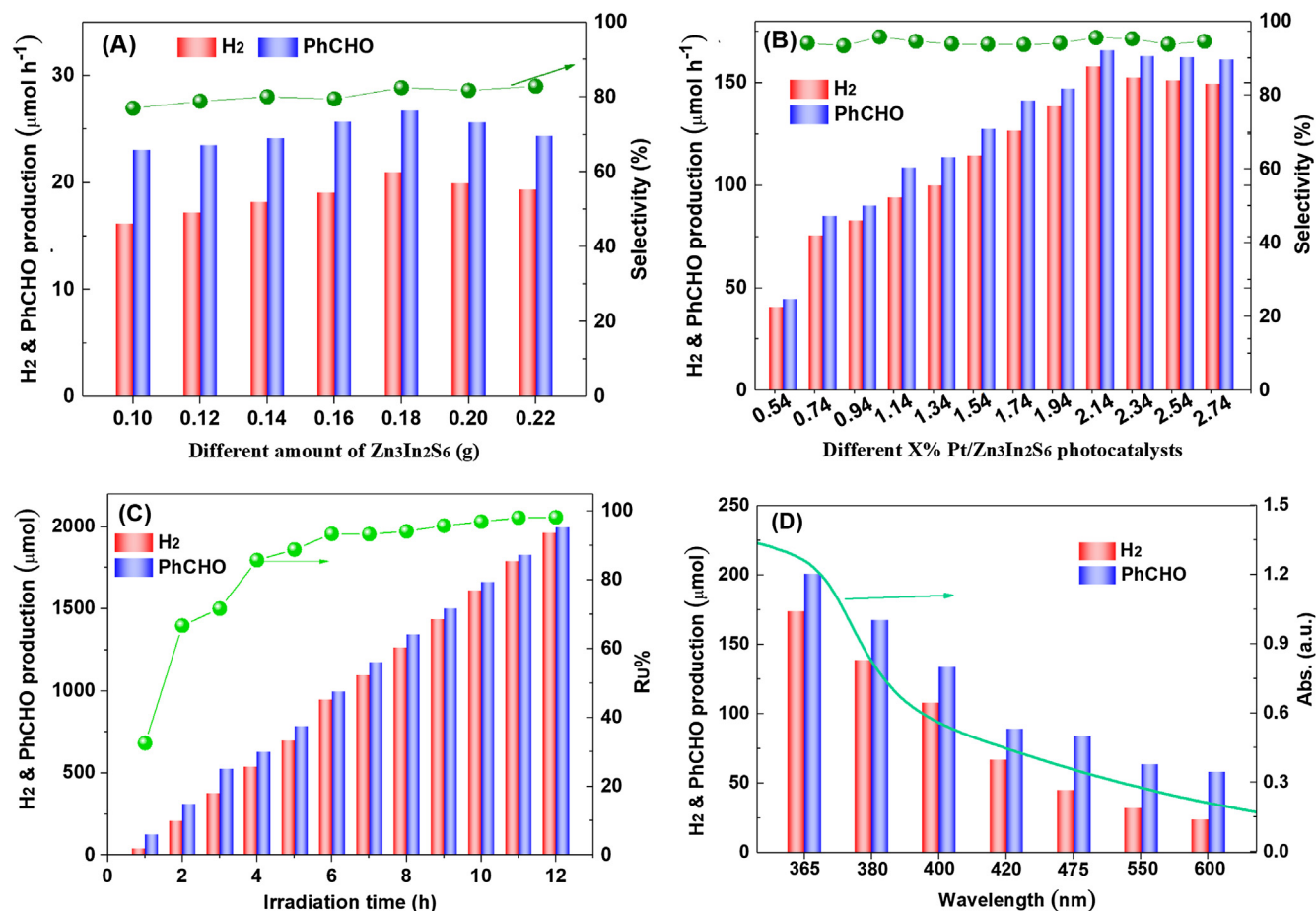


Fig. 6. Photocatalytic splitting of PhCH₂OH for H₂ evolution and PhCHO production and PhCHO selectivity over (A) different amount of Zn₃In₂S₆ and (B) Pt/Zn₃In₂S₆ hybrid with different weight content of Pt under visible light irradiation. (C) Photocatalytic splitting of PhCH₂OH for H₂ evolution and PhCHO production and the molar ratio of H₂ and PhCHO (R_H) over 2.14% Pt/Zn₃In₂S₆ hybrid under visible light irradiation. (D) UV-vis DRS spectrum of 2.14% Pt/Zn₃In₂S₆ hybrid and activity of 2.14% Pt/Zn₃In₂S₆ hybrid for photocatalytic splitting of PhCH₂OH under different incident lights.

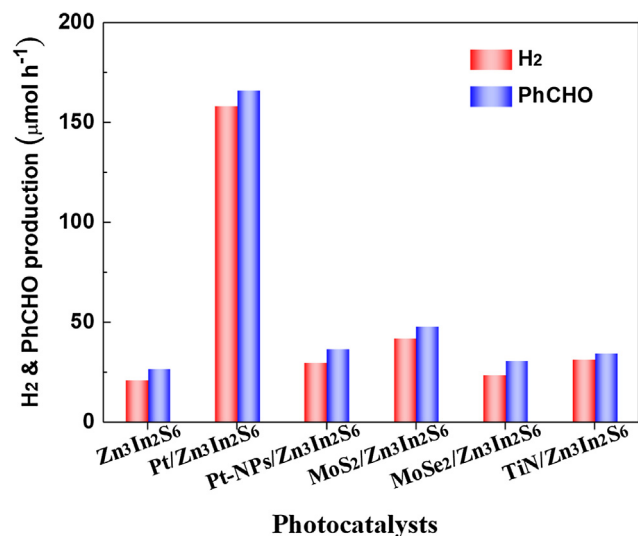


Fig. 7. Comparison of Zn₃In₂S₆, 2.14% Pt/Zn₃In₂S₆, 1% Pt-NPs/Zn₃In₂S₆, 1% MoS₂/Zn₃In₂S₆, 1% MoSe₂/Zn₃In₂S₆ and 1% TiN/Zn₃In₂S₆ photocatalysts for photocatalytic splitting of PhCH₂OH for H₂ evolution and PhCHO production.

of the aromatic aldehydes are relatively low due to electron-withdrawing effect [42], but the corresponding selectivity is high because of metal-support interactions (see the following mechanism discussion) [45,50].

To illustrate the general applicability of this dual-function photocatalytic reaction system for other photocatalysts, two hot photocatalysts (CdS and ZnIn₂S₄) studied for photocatalytic H₂ evolution were prepared. As shown in Fig. S10, XRD analysis revealed that the as-synthesized metal sulfides are well crystallized. The as-prepared CdS and ZnIn₂S₄ can be well indexed to the hexagonal structures of CdS (JCPDS No. 41-1049) and ZnIn₂S₄ (JCPDS No. 65-2023), respectively. Moreover, the hexagonal CdS exhibits microsphere shape constituted by nanoparticles; the sample ZnIn₂S₄ shows a typical marigold-like morphology (Fig. S11). The photocatalytic activities of CdS, Pt/CdS, ZnIn₂S₄ and Pt/ZnIn₂S₄ for selective splitting of benzyl alcohol into corresponding benzaldehyde and H₂ are shown in Fig. S12. It can be seen that compared with pure metal sulfides, the photocatalytic activities (yields of benzaldehyde and H₂) of Pt/metal sulfide are all remarkably enhanced. It is demonstrated that visible light-driven splitting of aromatic alcohols into hydrogen and corresponding aldehydes could be achieved on usual photocatalysts.

In the traditional solar-driven CO₂ reduction, the photogenerated electrons are reacted with CO₂ to produce chemicals, while the photogenerated holes are wasted by hole-scavengers [44]. Thus, this proposed strategy would also be extended in the photocatalytic reduction of CO₂, that is simultaneously visible-light-driven CO₂ reduction and selective oxidation of alcohols were performed in one reaction system. The experimental details were enclosed in the supporting information. The result show that the deoxygenative CO₂ reduction with CO-evolving and the

dehydrogenative alcohols oxidation with aldehydes-producing could be realized in one reaction system under visible light irradiation. The production rates of PhCHO and CO are about 17.5 and 6.3 $\mu\text{mol h}^{-1}$, respectively. Therefore, there will be a big enough space and opportunity to establish the novel photocatalytic system for practical application such as H_2 production, reduction of CO_2 and N_2 fixation.

3.3. Mechanism

3.3.1. Mechanism of Pt_x formation

Based on the above characterization and analyses, the hybrid $\text{Pt}/\text{Zn}_3\text{In}_2\text{S}_6$ with 0D-2D-3D hierarchical structures could be successfully prepared by this facile in situ approach and is stable in the cooperative photoredox catalysis. It is known that the formation of noble metal nanocrystals generally involves two stages: nucleation and growth [19]. In a typical process, $[\text{PtCl}_6]^{2-}$ ions are reduced to Pt^0 atoms, which subsequently aggregate to generate nuclei, which then grow into nanocrystals via sequential reduction of $[\text{PtCl}_6]^{2-}$ into Pt^0 on the formed nuclei. In the previously reported photodeposition for preparing a stable atomically dispersed $\text{Pd}-\text{TiO}_2$ (Pd_1/TiO_2), formation of ethylene glycolate radicals on TiO_2 nanosheets by UV light irradiation could forestall growth of Pd_1 and was critical for fabrication of Pd_1/TiO_2 [46]. In this work, $[\text{PtCl}_6]^{2-}$ ions, the reactant (PhCH_2OH) and $\text{Zn}_3\text{In}_2\text{S}_6$ photocatalyst exposed (1 1 0) crystal plane co-existed in the cooperative photoredox reaction, as illustrated in Fig. 8. The crystal structure of hexagonal $\text{Zn}_3\text{In}_2\text{S}_6$ shows that lots of S atoms are exposed on (1 1 0) plane of $\text{Zn}_3\text{In}_2\text{S}_6$ nanosheets (Fig. 8A), which facilitate Pt atoms adsorbing and anchoring. Therefore, when the photoexcited electrons (reductant) are produced on the surface of $\text{Zn}_3\text{In}_2\text{S}_6$ via visible light irradiation, Pt^0 atoms are formed and anchored on the surface of $\text{Zn}_3\text{In}_2\text{S}_6$ by reaction of $[\text{PtCl}_6]^{2-}$ and photoexcited electrons (Fig. 8B). Consequently, the Schottky junction could be established by direct contact of semiconductor ($\text{Zn}_3\text{In}_2\text{S}_6$) with noble metal (Pt^0) and can act as a sink for the photoexcited electrons to facilitate the electrons from semiconductor to noble metal.

As shown in Fig. 9A, the computed work function of $\text{Zn}_3\text{In}_2\text{S}_6$ (3.6 eV) is lower than that of Pt (5.65 eV). Along with the formation of $\text{Pt}-\text{Zn}_3\text{In}_2\text{S}_6$ contact, an appropriate height of Schottky barrier (2.05 eV) between $\text{Zn}_3\text{In}_2\text{S}_6$ and Pt is formed due to the difference between the work function of $\text{Zn}_3\text{In}_2\text{S}_6$ and the work function of Pt

(Fig. 9B). Under visible light irradiation, the photoexcited electrons in the $\text{Zn}_3\text{In}_2\text{S}_6$ with a lower work function flow into the Pt with a higher work function. Moreover, the as-formed Schottky barrier can act as a sink for the photogenerated electrons to inhibit the backflow of electrons from the Pt to the $\text{Zn}_3\text{In}_2\text{S}_6$. Such a $\text{Pt}/\text{Zn}_3\text{In}_2\text{S}_6$ Schottky junction thus boosts the flow of electrons from the $\text{Zn}_3\text{In}_2\text{S}_6$ to the Pt and leaves holes in the $\text{Zn}_3\text{In}_2\text{S}_6$, preventing the recombination of photogenerated electrons and holes (Fig. 9C). On the other hand, it has been well assigned that metallic Pt^0 is an effective co-catalyst for photocatalytic reduction H^+ into H_2 [13–15], which was also proved in this work (see photoactivity analysis). Thus the electrons on the Pt^0 atoms would be robbed by H^+ to form H_2 , which inhibits (or completes with) the $[\text{PtCl}_6]^{2-}$ ions are further reduced on the formed Pt^0 atoms and prevents its growth. Thus, 2D $\text{Zn}_3\text{In}_2\text{S}_6$ nanoflakes decorated with atomically dispersed Pt_x ($x = 1-4$) are formed in the photocatalytic reaction.

3.3.2. Mechanism of enhanced photocatalytic activity

It is known that in the photocatalytic process, a photocatalyst could be photoexcited by the induced light with energy larger than the band-gap energy of the photocatalyst to produce the photoexcited charges (electrons and holes), which then separate and transfer on the surface of the photocatalyst to react with reactant molecules [29,56–58]. Therefore, the photocatalytic performance of a photocatalyst is influenced by many factors such as crystalline phase, morphology, light absorption, and the photoexcited charges separation and transportation, etc., among which the last one is documented to be the most crucial factor [31–35]. Herein, after deposition of Pt_x on $\text{Zn}_3\text{In}_2\text{S}_6$, the crystallographic and microscopic structures of $\text{Pt}/\text{Zn}_3\text{In}_2\text{S}_6$ hybrid are the same as pure $\text{Zn}_3\text{In}_2\text{S}_6$. Consequently, photoluminescence (PL) and photoelectrochemical experiments were carried out to study the charge production, separation and transportation [59–62]. The PL spectra in Fig. 10A exhibit a broad emission peak, which is assigned to the recombination of the photogenerated electrons and holes. After deposition of Pt_x on $\text{Zn}_3\text{In}_2\text{S}_6$, the PL intensity of $\text{Pt}/\text{Zn}_3\text{In}_2\text{S}_6$ hybrid become weak compared with that of pure $\text{Zn}_3\text{In}_2\text{S}_6$. It is attributed to the fact that noble metal Pt_x can act as a sink to trap the photogenerated electrons from $\text{Zn}_3\text{In}_2\text{S}_6$ (Fig. 9), thus suppressing the undesirable recombination process of the photogenerated electrons and holes. Importantly, the introduction of Pt_x results in rapid charge transfer in the $\text{Pt}/\text{Zn}_3\text{In}_2\text{S}_6$ hybrid compared with pure $\text{Zn}_3\text{In}_2\text{S}_6$, as

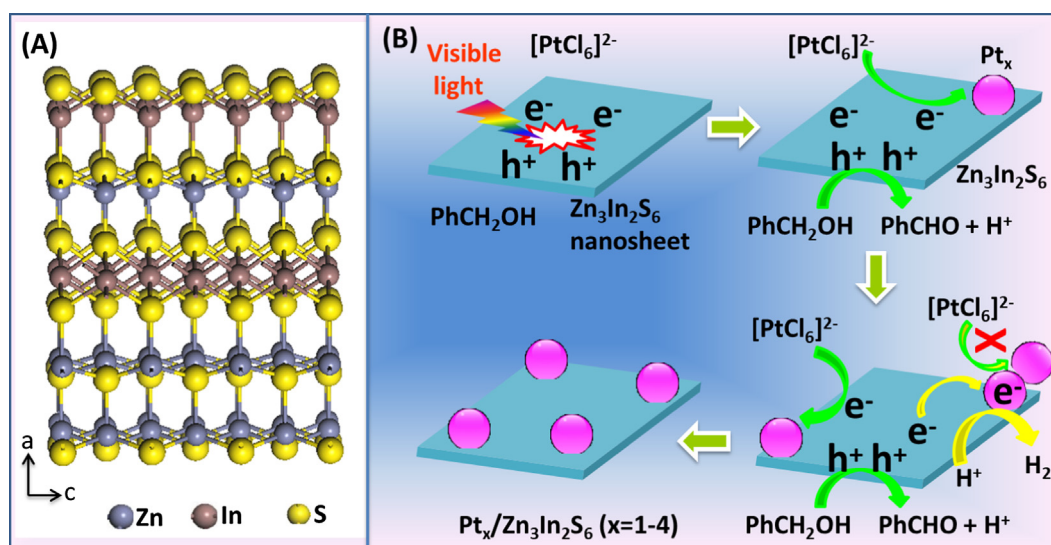


Fig. 8. (A) The crystal structure of hexagonal $\text{Zn}_3\text{In}_2\text{S}_6$ exposed (1 1 0) plane (topside). (B) Pictorial representation of the process for in situ fabrication of the $\text{Pt}_x/\text{Zn}_3\text{In}_2\text{S}_6$ hybrid.

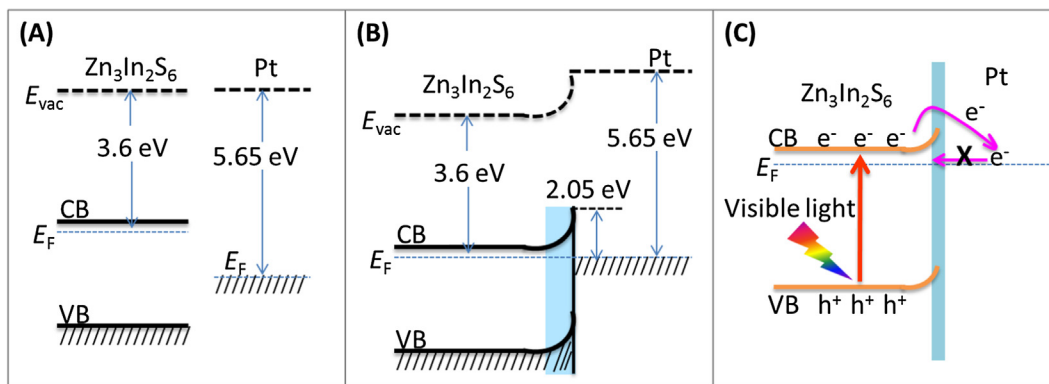


Fig. 9. Energy level lineup diagrams for $\text{Zn}_3\text{In}_2\text{S}_6$ and Pt (A) before and (B) after interfacing. (C) Schematic band diagram illustrating the charge transfer driven by the Schottky junction (CB, VB, e^- and h^+ are conduction band, valence band, photogenerated electrons and holes of $\text{Zn}_3\text{In}_2\text{S}_6$, respectively. E_{vac} and E_{F} denote vacuum level and Fermi level, respectively.).

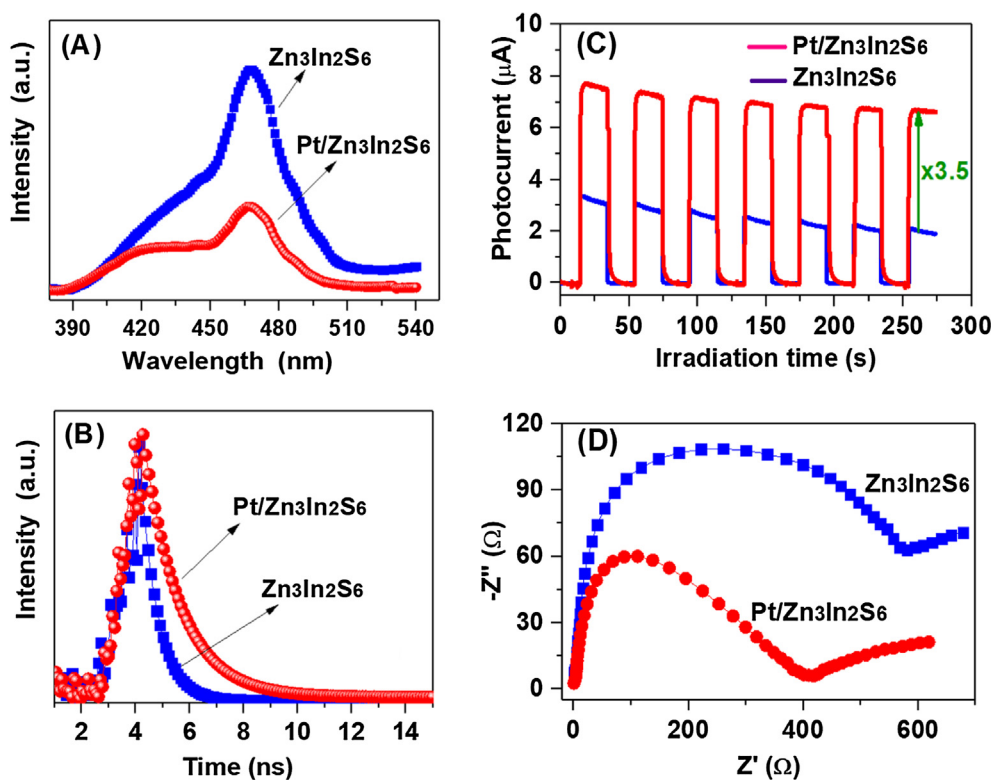


Fig. 10. (A) Steady-state PL spectra and (B) time-resolved PL spectra of $\text{Zn}_3\text{In}_2\text{S}_6$ and 2.14% Pt/ $\text{Zn}_3\text{In}_2\text{S}_6$ samples. (C) Transient photocurrent response of $\text{Zn}_3\text{In}_2\text{S}_6$ and 2.14% Pt/ $\text{Zn}_3\text{In}_2\text{S}_6$ electrodes in 0.1 M Na_2SO_4 solution without bias versus Ag/AgCl under visible light irradiation. (D) EIS Nyquist plots of $\text{Zn}_3\text{In}_2\text{S}_6$ and 2.14% Pt/ $\text{Zn}_3\text{In}_2\text{S}_6$ samples in 0.1 M KCl solution containing 0.1 M $\text{K}_3[\text{Fe}(\text{CN})_6]/\text{K}_4[\text{Fe}(\text{CN})_6]$.

confirmed by time-resolved PL spectroscopy tests. The average PL lifetimes of Pt/ $\text{Zn}_3\text{In}_2\text{S}_6$ hybrid and pure $\text{Zn}_3\text{In}_2\text{S}_6$ are 1.3 and 0.7 ns, respectively (Fig. 10B). Moreover, the high efficiency of the charge production, separation and transportation on Pt/ $\text{Zn}_3\text{In}_2\text{S}_6$ hybrid can also be confirmed by photoelectrochemical measurements. As shown in Fig. 10C, the generation of an enhanced photocurrent for Pt/ $\text{Zn}_3\text{In}_2\text{S}_6$ hybrid, which is about 3.5 times higher than that of pure $\text{Zn}_3\text{In}_2\text{S}_6$, obviously illustrates that the production and mobility of the charge are promoted. Consistently, the electrochemical impedance spectroscopy (EIS) study of the charge transfer rate reveals the expected semicircular Nyquist plots for pure $\text{Zn}_3\text{In}_2\text{S}_6$ and Pt/ $\text{Zn}_3\text{In}_2\text{S}_6$ hybrid (Fig. 10D). EIS data are analyzed in terms of an equivalent circuit model, and the values of charge transfer resistance are about 416 and 580 Ω/cm^2

for Pt/ $\text{Zn}_3\text{In}_2\text{S}_6$ hybrid and pure $\text{Zn}_3\text{In}_2\text{S}_6$, respectively. The linear-sweep voltammograms of the $\text{Zn}_3\text{In}_2\text{S}_6$ and 2.14% Pt/ $\text{Zn}_3\text{In}_2\text{S}_6$ photoelectrodes under visible light irradiation were also detected (Fig. S13). The cathodic current found in the range of -0.6 to -1.3 V (vs Ag/AgCl) can be attributed to H_2 evolution. The significantly enhanced photocurrent of the 2.14% Pt/ $\text{Zn}_3\text{In}_2\text{S}_6$ hybrid in comparison with the pure $\text{Zn}_3\text{In}_2\text{S}_6$ indicates a more effective separation of photogenerated electrons and holes over the 2.14% Pt/ $\text{Zn}_3\text{In}_2\text{S}_6$ hybrid.

On the above analysis, Pt/ $\text{Zn}_3\text{In}_2\text{S}_6$ hybrid exhibits higher visible light absorption than pure $\text{Zn}_3\text{In}_2\text{S}_6$ (Fig. 2), which could facilitate the production of the visible-light photoexcited charges. Additionally, the atomically dispersed Pt_x can be prepared on the active sites of $\text{Zn}_3\text{In}_2\text{S}_6$ and intimate contacts with it by this in situ

photo-deposition method (Fig. 4), which can promote separation and transportation of the photogenerated charges (Fig. 10). Moreover, the atomically dispersed Pt_x could offer the maximum atom efficiency and provide more reactive sites in comparison with Pt nanoparticles (NPs). Thus, the reaction kinetics could be improved significantly and resulting in enhancement of photoactivity. The pure Zn₃In₂S₆ exhibits relative low selectivity due to generation of a small quantity of deoxidized product in the photocatalytic reaction via electron reduction [25]. However, negligible deoxidized product was detected on the Pt/Zn₃In₂S₆ hybrid. The high selectivity can be attributed to the intrinsic properties of atomic Pt cocatalyst and metal-support interactions [45,50]. The enhanced selectivity on the Pt/Zn₃In₂S₆ hybrid could be attributed to the fact that the photogenerated electrons can be effectively separated and transferred to the atomically dispersed Pt and the atomically dispersed Pt can improve the reaction kinetics of H₂ evolution significantly (it has the largest work function and the lowest overpotential for H₂ evolution). Therefore, the electrons will react with

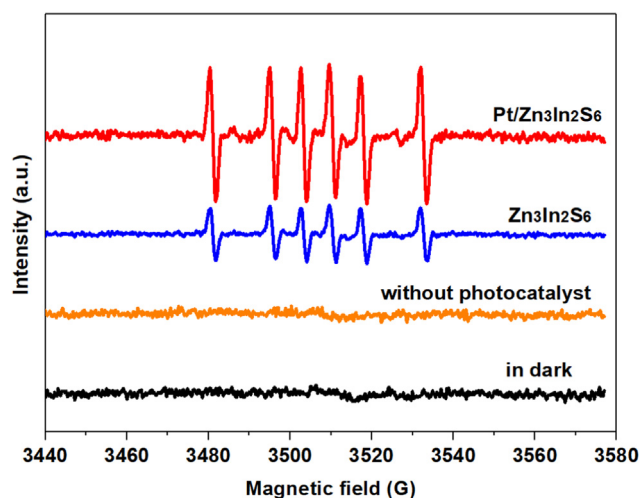


Fig. 11. EPR detection of in-situ formed carbon-centered radicals under different reaction conditions.

protons to form H₂ but not deoxidized product of alcohols. These encouraging results strongly demonstrate that the atomic Pt_x can effectively promote the production, separation and transfer of the photogenerated charges, and eventually result in higher photocatalytic activity and selectivity of the Pt/Zn₃In₂S₆ hybrid than that of pure Zn₃In₂S₆ toward simultaneous RPhCHO production and H₂ evolution in one reaction system under visible light irradiation.

3.3.3. Mechanism of photocatalytic redox reaction

To understand the process of photocatalytic splitting of PhCH₂OH over Pt/Zn₃In₂S₆ hybrid, a radical trapping experiment and an isotopic labelling study were performed. As shown in Fig. 11, six EPR peaks over both Zn₃In₂S₆ and Pt/Zn₃In₂S₆ hybrid emerged when DMPO was added into the reaction system under visible light irradiation. They can be assigned to carbon-centered radicals [25]. However, no EPR signals were detected on the blank tests (the reaction system with the addition of DMPO in the dark; the reaction system with the addition of DMPO but without photocatalyst under visible light irradiation), indicating that the process of splitting of PhCH₂OH is truly triggered by visible-light-driven photocatalysis. It is consistent with the above photoactivity test. Additionally, the intensity of the EPR signal over Pt/Zn₃In₂S₆ hybrid is obviously stronger than that over pure Zn₃In₂S₆, demonstrating that much more carbon-centered radicals are formed after deposition of Pt_x on Zn₃In₂S₆. This also proves that the Pt_x can effectively promote the separation and transfer of the photogenerated charges, because photogenerated holes make contributions to the formation of carbon-centered radicals. Fig. S14 shows mass spectra of PhCD₂OH (*m/z* = 110) and its product (benzaldehyde) over Pt/Zn₃In₂S₆ hybrid. It can be seen that the dehydrogenation product is PhCDO (*m/z* = 107) when PhCD₂OH was introduced in the reaction system instead of PhCH₂OH. It demonstrates that H atoms of O–H and α C–H are dehydrogenated in the photocatalytic reaction.

Therefore, on the basis of the above experimental results and analysis, a possible reaction mechanism for photocatalytic splitting of PhCH₂OH by Pt/Zn₃In₂S₆ hybrid with simultaneous H₂ evolution and PhCHO production under visible light irradiation was proposed. As illustrated in Fig. 12, the semiconductor Zn₃In₂S₆ is firstly excited by visible light and generates photoexcited electron-hole

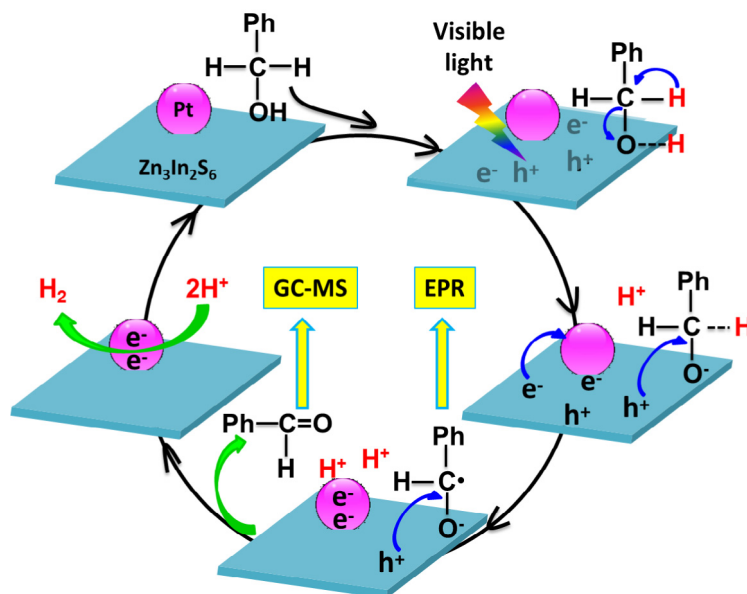


Fig. 12. Proposed reaction mechanism of the photocatalytic splitting of PhCH₂OH by Pt/Zn₃In₂S₆ hybrid for simultaneous H₂ evolution and PhCHO production under visible light irradiation.

pairs. The electrons are transferred from the conduction band of $\text{Zn}_3\text{In}_2\text{S}_6$ to the deposited Pt_x due to the presence of the Schottky junction, leaving the holes in the valence band of $\text{Zn}_3\text{In}_2\text{S}_6$. An adsorbed PhCH_2OH molecule is deprotonated to form one H^+ ion (from OH group) and an alkoxide anion, and then reacts with a photogenerated hole, affording one corresponding carbon radical and one H^+ ion (from the α C–H of PhCH_2O group). This carbon radical further reacts with one photogenerated hole to produce a PhCHO molecule. Simultaneously, two dehydrogenated H^+ ions react with two photogenerated electrons accumulated in the Pt_x to evolve a H_2 molecule. In this cooperative photoredox reaction, photocatalytic selective oxidation reaction consumes one PhCH_2OH molecule and two holes, and produces one PhCHO molecule and two protons; photocatalytic selective reduction process depletes two electrons and two protons, and affords one H_2 molecule. Therefore, a cycle and efficient solar-to-chemical energy conversion of biomass-relevant substrates reaction system was established.

4. Conclusions

In summary, the 3D microsphere $\text{Zn}_3\text{In}_2\text{S}_6$ assembled by 2D $\text{Zn}_3\text{In}_2\text{S}_6$ nanoflakes decorated with atomic Pt_x ($x = 1-4$) can be prepared by the in situ photocatalytic reaction, and can be used as an efficient, dual-functional and visible-light-driven photocatalyst toward the photocatalytic selective splitting of aromatic alcohols into clean energy (H_2) and fine chemicals (aromatic aldehydes or ethers) simultaneously in one reaction system under mild reaction conditions. In the reaction system, the photogenerated electrons and holes were effectively used, and it shows much higher photocatalytic activity than two half-reactions: the photocatalytic selective oxidation under O_2 atmosphere and the water splitting with sacrificial reagents. The apparent quantum efficiency (AQE) for H_2 evolution at 400 nm over 2.14% $\text{Pt}/\text{Zn}_3\text{In}_2\text{S}_6$ hybrid could be achieved 4.6%. The Pt_x as a co-catalyst can effectively promote the production, separation and transfer of the photogenerated charges and eventually result in the significantly enhanced photocatalytic activity. Benzyl alcohol is first dehydrogenated into benzaldehyde and H^+ ions via the corresponding carbon-centered radical by photoexcited holes, then H^+ ions dehydrogenated from OH group and α C–H of benzyl alcohol are evolved into H_2 by photogenerated electrons. This study not only provides a promising way to directly use of photogenerated electrons and holes, but also supplies a dual-purpose, economic and sustainable way for synthesis of fine chemicals and H_2 evolution (or carbon dioxide reduction and nitrogen fixation).

Acknowledgement

This work was supported by the National Natural Science Foundation of China (NSFC, grant nos. 51472005, 51772118, 21473066 and 21603002), China; the Natural Science Foundation of Anhui Province, China (grant no. 1608085QB37); and the Natural Science Foundation of Educational Committee of Anhui Province (grant no. KJ2018A0387), China.

Appendix A. Supplementary material

Supplementary data associated with this article can be found, in the online version, at <https://doi.org/10.1016/j.jcat.2018.09.003>.

References

- [1] G.P. Peters, C.L. Quéré, R.M. Andrew, J.G. Canadell, P. Friedlingstein, T. Ilyina, R. B. Jackson, F. Joos, J.I. Korsbakken, G.A. McKinley, S. Sitch, P. Tans, *Nat. Clim. Change* 7 (2017) 848.
- [2] J. Murray, D. King, *Nature* 481 (2012) 433.

- [3] X. Chen, S. Shen, L. Guo, S.S. Mao, *Chem. Rev.* 110 (2010) 6503.
- [4] Y.K. Kim, H. Park, *Energy Environ. Sci.* 4 (2011) 685.
- [5] K.S. Lakhi, D.-H. Park, K. Al-Bahily, W. Cha, B. Viswanathan, J.-H. Choy, A. Vinu, *Chem. Soc. Rev.* 46 (2017) 72.
- [6] K. Chang, X. Hai, J. Ye, *Adv. Energy Mater.* 6 (2016) 1502555.
- [7] D.W. Wakerley, M.F. Kuehnel, K.L. Orchard, K.H. Ly, T.E. Rosser, E. Reisner, *Nat. Energy* 2 (2017) 17021.
- [8] K. Shimura, H. Yoshida, *Energy Environ. Sci.* 4 (2011) 2467.
- [9] V.S. Thoi, Y. Sun, J.R. Long, C.J. Chang, *Chem. Soc. Rev.* 42 (2013) 2388.
- [10] Y. Ma, X. Wang, Y. Jia, X. Chen, H. Han, C. Li, *Chem. Rev.* 114 (2014) 9987.
- [11] N. Zhang, C. Han, Y.-J. Xu, J.J. Foley IV, D. Zhang, J. Codrington, S.K. Gray, Y. Sun, *Nat. Photon.* 10 (2016) 473.
- [12] Y.-J. Yuan, Z.-T. Yu, D.-Q. Chen, Z.-G. Zou, *Chem. Soc. Rev.* 46 (2017) 603.
- [13] H. Yan, J. Yang, G. Ma, G. Wu, X. Zong, Z. Lei, J. Shi, C. Li, *J. Catal.* 266 (2009) 165.
- [14] X. Jiang, X. Fu, L. Zhang, S. Meng, S. Chen, *J. Mater. Chem. A* 3 (2015) 2271.
- [15] M. Xing, B. Qiu, M. Du, Q. Zhu, L. Wang, J. Zhang, *Adv. Funct. Mater.* 27 (2017) 1702624.
- [16] W. Yang, L. Zhang, J. Xie, X. Zhang, Q. Liu, T. Yao, S. Wei, Q. Zhang, Y. Xie, *Angew. Chem. Int. Ed.* 55 (2016) 6716.
- [17] B. Weng, Z. Xiao, W. Meng, C.R. Grice, T. Poudel, X. Deng, Y. Yan, *Adv. Energy Mater.* 7 (2017) 1602260.
- [18] H. Lu, J. Zhao, L. Li, L. Gong, J. Zheng, L. Zhang, Z. Wang, J. Zhang, Z. Zhu, *Energy Environ. Sci.* 4 (2011) 3384.
- [19] B. Weng, Q. Quan, Y.-J. Xu, *J. Mater. Chem. A* 4 (2016) 18366.
- [20] J. Kennedy, A. Datye, *J. Catal.* 179 (1998) 375.
- [21] K.K. Sakimoto, A.B. Wong, P. Yang, *Science* 351 (2016) 74.
- [22] K.A. Brown, D.F. Harris, M.B. Wilker, A. Rasmussen, N. Khadka, H. Hamby, S. Keable, G. Dukovic, J.W. Peters, L.C. Seefeldt, P.W. King, *Science* 352 (2016) 448.
- [23] C. Huang, C. Chen, M. Zhang, L. Lin, X. Ye, S. Lin, M. Antonietti, X. Wang, *Nat. Commun.* 6 (2015) 7698.
- [24] X. Ning, S. Meng, X. Fu, X. Ye, S. Chen, *Green Chem.* 18 (2016) 3628.
- [25] S. Meng, X. Ning, S. Chang, X. Fu, X. Ye, S. Chen, *J. Catal.* 357 (2018) 247.
- [26] X. Xiao, J. Jiang, L. Zhang, *Appl. Catal. B-Environ.* 142 (2013) 487.
- [27] N. Zhang, M. Yang, S. Liu, Y. Sun, Y.-J. Xu, *Chem. Rev.* 115 (2015) 10307.
- [28] X. Lang, J. Zhao, X. Chen, *Angew. Chem. Int. Ed.* 55 (2016) 4697.
- [29] X. Lang, J. Zhao, X. Chen, *Chem. Soc. Rev.* 45 (2016) 3026.
- [30] J.C. Colmenares, R. Luque, *Chem. Soc. Rev.* 43 (2014) 765.
- [31] G. Palmisano, V. Augugliaro, M. Pagliaro, L. Palmisano, *Chem. Commun.* 33 (2007) 3425.
- [32] A. Maldotti, A. Molinari, R. Amadelli, *Chem. Rev.* 102 (2002) 3811.
- [33] M. Zhang, Q. Wang, C. Chen, L. Zang, W. Ma, J. Zhao, *Angew. Chem. Int. Ed.* 48 (2009) 6081.
- [34] S. Yurdakal, G. Palmisano, V. Lodo, V. Augugliaro, L. Palmisano, *J. Am. Chem. Soc.* 130 (2008) 1568.
- [35] X. Lang, X. Chen, J. Zhao, *Chem. Soc. Rev.* 43 (2014) 473.
- [36] T.P.A. Ruberu, N.C. Nelson, I.I. Slowing, J. Vela, *J. Phys. Chem. Lett.* 3 (2012) 2798.
- [37] H. Zhang, Z. Zhu, Y. Wu, T. Zhao, L. Li, *Green Chem.* 16 (2014) 4076.
- [38] H. Zhang, Y. Wu, L. Li, Z. Zhu, *ChemSusChem* 8 (2015) 1226.
- [39] D. Jiang, X. Chen, Z. Zhang, L. Zhang, Y. Wang, Z. Sun, R.M. Irfan, P. Du, *J. Catal.* 357 (2018) 147.
- [40] Z. Chai, T.-T. Zeng, Q. Li, L.-Q. Lu, W.-J. Xiao, D. Xu, *J. Am. Chem. Soc.* 138 (2016) 10128.
- [41] I. Poullos, N. Papadopoulos, *Sol. Energy. Mater.* 20 (1990) 43.
- [42] J. Zhang, S. Meng, X. Ye, C. Ling, S. Zhang, X. Fu, S. Chen, *Appl. Catal. B-Environ.* 218 (2017) 420.
- [43] S. Shen, L. Zhao, L. Guo, *Int. J. Hydrogen Energy* 35 (2010) 10148.
- [44] S. Wang, B.Y. Guan, Y. Lu, X.W. Lou, *J. Am. Chem. Soc.* 139 (2017) 17305.
- [45] N. Zhang, C. Han, X. Fu, Y.-J. Xu, *Chem* 4 (2018) 1832.
- [46] P. Liu, Y. Zhao, R. Qin, S. Mo, G. Chen, L. Gu, D.M. Chevier, P. Zhang, Q. Guo, D. Zang, B. Wu, G. Fu, N. Zheng, *Science* 352 (2016) 797.
- [47] N. Naneshvar, D. Salari, A.R. Khataee, *J. Photo. Photobio. A* 162 (2004) 317.
- [48] B. Weng, K.-Q. Lu, Z. Tang, H.M. Chen, Y.-J. Xu, *Nat. Commun.* 9 (2018) 1543.
- [49] J.M. Thomas, K.D.M. Harris, *Energy Environ. Sci.* 9 (2016) 687.
- [50] T. Deng, W. Zheng, W. Zhang, *Chinese J. Catal.* 38 (2017) 1489.
- [51] X. Wu, H. Zhang, J. Dong, M. Qiu, J. Kong, Y. Zhang, Y. Li, G. Xu, J. Zhang, J. Ye, *Nano Energy* 45 (2018) 109.
- [52] H. Wei, X. Liu, A. Wang, L. Zhang, B. Qiao, X. Yang, Y. Huang, S. Miao, J. Liu, T. Zhang, *Nat. Commun.* 5 (2014) 5634.
- [53] C.J. Jiang, J.M. Elliott, D.J. Cardin, S.C. Tsang, *Langmuir* 25 (2008) 534.
- [54] M. Yu, S. Zhao, H. Feng, L. Hu, X. Zhang, Y. Zeng, Y. Tong, X. Lu, *ACS Energy Lett.* 2 (2017) 1862.
- [55] S. Deng, Y. Zhong, Y. Zeng, Y. Wang, Z. Yao, F. Yang, S. Lin, X. Wang, X. Lu, X. Xia, *J. Tu, Adv. Mater.* 29 (2017) 1700748.
- [56] X. Lu, S. Xie, H. Yang, Y. Tong, H. Ji, *Chem. Soc. Rev.* 43 (2014) 7581.
- [57] P. Zhou, J. Yu, M. Jaroniec, *Adv. Mater.* 26 (2014) 4920.
- [58] M.R. Hoffmann, S.T. Martin, W. Choi, D.W. Bahnemann, *Chem. Rev.* 95 (1995) 69.
- [59] S. Wang, B.Y. Guan, X.W. Lou, *J. Am. Chem. Soc.* 140 (2018) 5037.
- [60] J. Zhang, F.-X. Xiao, *J. Mater. Chem. A* 5 (2017) 23681.
- [61] X. Jiao, Z. Chen, X. Li, Y. Sun, S. Gao, W. Yan, C. Wang, Q. Zhang, Y. Lin, L. Luo, Y. Xie, *J. Am. Chem. Soc.* 139 (2017) 7586.
- [62] K.-Q. Lu, X. Xin, N. Zhang, Z.-R. Tang, Y.-J. Xu, *J. Mater. Chem. A* 6 (2018) 4590.